Vectorial insertion of apical and basolateral membrane proteins in polarized epithelial cells revealed by quantitative 3D live cell imaging

Wei Hua,[1] David Sheff,[2] Derek Toomre,[1] and Ira Mellman[1]

[1]Department of Cell Biology, Ludwig Institute for Cancer Research, Yale University School of Medicine, New Haven, CT 06520
[2]Department of Pharmacology, The University of Iowa, Iowa City, IA 52242

Although epithelial cells are known to exhibit a polarized distribution of membrane components, the pathways responsible for delivering membrane proteins to their appropriate domains remain unclear. Using an optimized approach to three-dimensional live cell imaging, we have visualized the transport of newly synthesized apical and basolateral membrane proteins in fully polarized filter-grown Madin–Darby canine kidney cells. We performed a detailed quantitative kinetic analysis of trans-Golgi network (TGN) exit, passage through transport intermediates, and arrival at the plasma membrane using cyan/yellow fluorescent protein–tagged glycosylphosphatidylinositol-anchored protein and vesicular stomatitis virus glycoprotein as apical and basolateral reporters, respectively. For both pathways, exit from the TGN was rate limiting. Furthermore, apical and basolateral proteins were targeted directly to their respective membranes, resolving current confusion as to whether sorting occurs on the secretory pathway or only after endocytosis. However, a transcytotic protein did reach the apical surface after a prior appearance basolaterally. Finally, newly synthesized proteins appeared to be delivered to the entire lateral or apical surface, suggesting—contrary to expectations—that there is not a restricted site for vesicle docking or fusion adjacent to the junctional complex.

Introduction

Epithelial cells are characterized by the asymmetric distribution of plasma membrane proteins to form apical and basolateral domains. Many membrane proteins are thought to reach their respective domains by intracellular sorting events mediated by distinctive targeting elements (Matter and Mellman, 1994; Mostov et al., 2003; Rodriguez-Boulan et al., 2005). For example, many apical proteins, including those with glycosylphosphatidylinositol (GPI) membrane anchors, are sorted into clustered lipid rafts and traffic to the apical surface (Lisanti et al., 1989; Paladino et al., 2004; Schuck and Simons, 2004). In contrast, many basolateral proteins, such as low density lipoprotein receptor and vesicular stomatitis virus glycoprotein (VSVG), are sorted as a result of the recognition of signals localized in the cytoplasmic tail (Matter and Mellman, 1994). The protein components responsible for at least some basolateral sorting events, such as the AP–1B clathrin adaptor complex, are beginning to be discovered (Folsch et al., 1999; Simmen et al., 2002; Folsch, 2005). However, the actual pathways of polarized membrane protein trafficking, including the identity or location of sorting sites, the itinerary taken by individual proteins, and the spatial distribution of plasma membrane delivery sites, remain largely unresolved.

Polarized membrane protein sorting on the secretory pathway has long been presumed to occur at the TGN (Griffiths et al., 1985; Keller et al., 2001), although the closely associated recycling endosomes also appear to play an important role (Gan et al., 2002; Ang et al., 2003, 2004; Folsch et al., 2003). Recently, however, questions have emerged concerning the extent to which polarized sorting even occurs intracellularly (Nelson and Rodriguez-Boulan, 2004). In one study, the transport of polarized membrane proteins was assayed in MDCK cells whose apical or basolateral surface had been selectively inactivated by tannic acid fixation. Striking images suggested that a well-characterized reporter of apical proteins, a GPI-anchored GFP (GPI-GL-YFP), was first inserted into the basolateral surface and transcytosed across the cell to reach the apical domain (Polishchuk et al., 2004). Although inconsistent with some classic biochemical studies (Matlin and Simons, 1984; Lisanti

Correspondence to Ira Mellman: ira.mellman@yale.edu

Abbreviations used in this paper: 3D, three dimensional; GPI, glycosylphosphatidylinositol; VSVG, vesicular stomatitis virus glycoprotein.

The online version of this article contains supplemental material.

The Journal of Cell Biology, Vol. 172, No. 7, March 27, 2006 1035–1044
http://www.jcb.org/cgi/doi/10.1083/jcb.200512012

et al., 1990; Matter et al., 1990), this indirect pathway is reminiscent of what is thought to occur for many apical proteins in hepatocytes (Bartles et al., 1987). In MDCK cells, however, apical proteins bearing conventional membrane anchors were suggested to take the classic direct route (Lipardi et al., 2000; Polishchuk et al., 2004; Schuck and Simons, 2004; Anderson et al., 2005).

It remains similarly unclear whether membrane proteins insert at specific sites on the apical or basolateral surfaces. Junctional complexes have been suggested to define a spatially restricted insertion site for basolateral traffic based on the distribution of tethering complexes (Sec6–Sec8) involved in vesicle docking at the basolateral membrane (Grindstaff et al., 1998). However, the only direct evidence from live cell imaging experiments thus far is that basolateral proteins do not first appear at the adherent surface of coverslip-grown MDCK cells (Kreitzer et al., 2003). Some transport vesicles were seen to enter the junctional complex region, but definitive evidence for vesicle fusion to the plasma membrane or a quantitative assessment of vesicle traffic to this domain of the lateral surface was not achieved. Such considerations have emphasized the need for visualizing the biosynthetic pathway of membrane proteins in filter-grown and fully polarized epithelial cells. Although this approach has thus far proved challenging because of the cells' z-axis height (~10 μm; Keller et al., 2001), we have now been able to image and quantify the features of secretory membrane traffic in live, unperturbed MDCK cells.

Results

By combining laser scanning confocal microscopy with rapid data acquisition and computation, we were able to visualize and quantitate polarized membrane protein traffic in filter-grown MDCK cells for a period of ~30 min. As a test, we first studied the intracellular sorting and insertion of a basolateral membrane protein, ts045 VSVG-YFP (Keller et al., 2001). VSVG-YFP

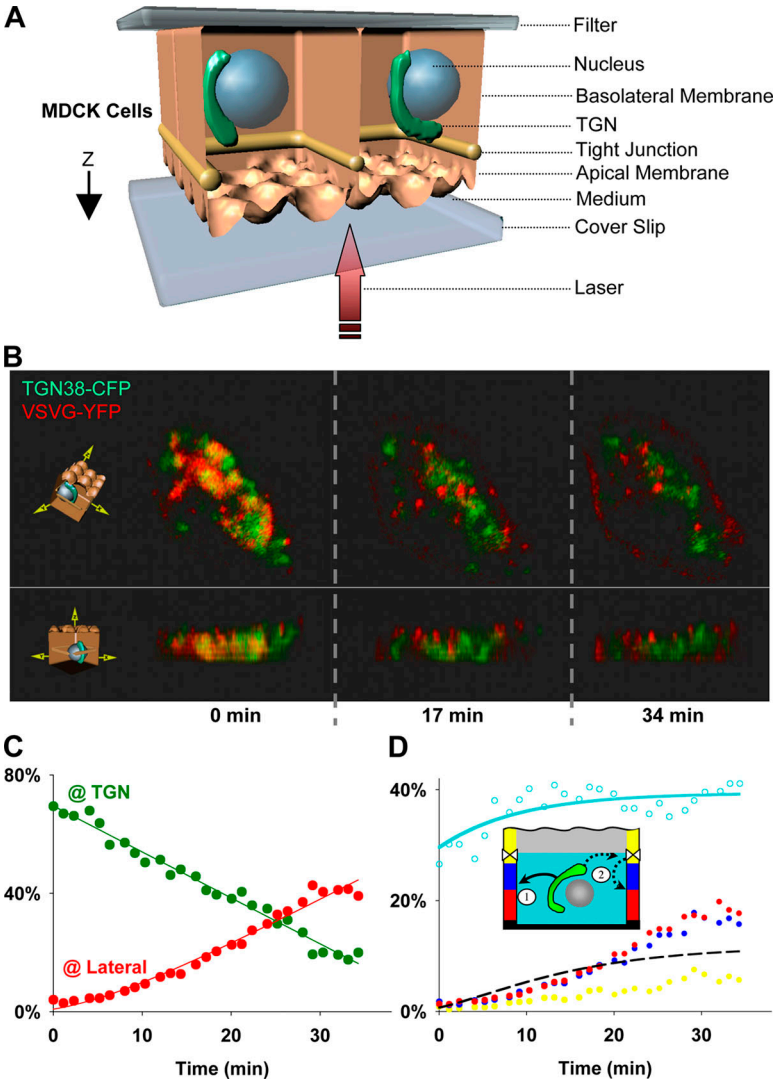

Figure 1. **3D time-lapse confocal imaging and quantification of the transport of VSVG-YFP to the basolateral surface in single fully polarized MDCK cells.** (A) Illustration of the MDCK cell domains and orientation for 3D live cell imaging. MDCK cells were grown on polycarbonate filters and transfected as described in Materials and methods. A piece of filter was excised and inverted on a coverslip in a medium-filled dish. The dish was placed in a temperature-controlled chamber mounted on a laser scanning confocal microscope. (B) 3D transport of newly synthesized VSVG-YFP from the TGN to the basolateral membrane. Transport from the TGN (marked by TGN38-CFP, green) was monitored at 31°C, with complete z-axis stacks taken every minute. Individual stacks were assembled as videos. Here, the same cell is viewed from two different orientations (looking down from the apical side and from the lateral side), as illustrated by the 3D cell diagram, at three time points of chase: 0, 17, and 34 min. VSVG-YFP (red) at 0 min largely colocalized with the TGN marker and gradually exited from the TGN to appear at the lateral surface (Video 1, available at http://www.jcb.org/cgi/content/full/jcb.200512012/DC1). (C) Kinetics of VSVG-YFP transport from the TGN to the lateral surface (same cell as in B.). The presence of VSVG-YFP in the TGN (TGN38-CFP–positive volumes, green dots) or at the lateral surface (including ~1.5 μm of adjacent cytoplasmic volume, red dots) was quantified from the 3D renderings. Global fit (solid lines) of the two-step pathway (Fig. 2, model 1) to the two curves yielded $k_1 = 0.02\ min^{-1}$, $k_2 = 0.11\ min^{-1}$, and $R^2 = 0.9857$. The data shown are collected from a single cell, and the rate constants are representative of measurements from 12 different cells as summarized in Fig. 2. (D) Spatial distribution of VSVG-YFP (same cell as in B and C). The distribution of VSVG-YFP on three equal vertical sections of the lateral membrane was determined at each time point from the 3D renderings. The Xs demarcate the approximate location of the tight junction. Each data point represents the percentage of VSVG-YFP present in the section of the diagrammed membrane and was color coded accordingly. The fluorescence in the apical-most segment (yellow dots) was lowest, but this region also contains a portion of the lateral domain that is apical to the junctional complex. The dashed line is the predicted fluorescence in the junction-associated region if VSVG-YFP was first inserted at this site, according to model 2 (Fig. 2), with $k_3 = 0.12\ min^{-1}$, the fastest sorting rate cited in polarized MDCK cells (Sheff et al., 2002). The yellow dots, which correspond to a portion of the apical region, deviate significantly from this prediction. Open cyan circles represent the amount of VSVG-YFP fluorescence at each time point that could not be accounted for either at the lateral membrane or in the TGN. Solid cyan line represents the fit to model 1 (Fig. 2). The dimensions of the cell image shown (x, y, and z) are ~12, 14, and 8 μm.

was transfected into MDCK cells expressing CFP-tagged TGN38 (TGN38-CFP; Keller et al., 2001) as markers for the TGN. VSVG-YFP was accumulated in the ER by incubation at 40°C overnight and was released and chased to the TGN by a 1-h incubation at 20°C (Griffiths et al., 1985). Synchronous cell surface transport was imaged by transferring the filters to the permissive temperature (31°C) on a temperature-controlled stage, mounted as shown in Fig. 1 A. The preparations remained viable for >12 h.

YFP and CFP fluorescent signals in single MDCK cells were collected in multiple z stacks over a 30–40-min time course and combined to produce three-dimensional (3D) videos (Video 1; available at http://www.jcb.org/cgi/content/full/jcb.200512012/DC1). 3D stacks were acquired at 1-min intervals to minimize photobleaching. At the start of the 31°C chase, most of the VSVG-YFP (Fig. 1 B, red) colocalized with TGN38-CFP (Fig. 1 B, green) as expected (Fig. 1 B, 0 min). VSVG-YFP then gradually exited from the TGN and appeared at the lateral membrane (Fig. 1 B, 17 and 34 min). As found previously for MDCK cells on glass coverslips (Kreitzer et al., 2003), VSVG was not observed reaching the basal (filter attached) domain of the plasma membrane; this domain was thus excluded from further analysis. Although the time resolution was not enough to allow tracking of individual transport vesicles, we noted only two significant accumulation sites of VSVG: the TGN region and the lateral membrane, suggesting that after exit from the TGN, there were no rate-limiting steps before plasma membrane appearance.

We next quantified the amount of VSVG-YFP in TGN and basolateral regions in the 3D renderings at each time point. Because all signals were within the linear range of the detector, the amount of VSVG-YFP was proportional to the fluorescence signal in any given region. Measurements were converted into percentages of total signal in the cell to compensate for photobleaching (determined separately for each probe; Fig. S1, available at http://www.jcb.org/cgi/content/full/jcb.200512012/DC1).

The amount of VSVG in the TGN region decreased concomitantly with the increase in the amount of VSVG at the lateral membrane (Fig. 1 C). TGN exit could be approximated by a linear decay curve, suggesting that the exit rate was independent of VSVG concentration. The rate of VSVG appearance at the lateral membrane increased after a brief lag (Fig. 1 C, red), suggesting at least one intermediate step before VSVG's plasma membrane arrival. To compute the kinetics of arrival at the lateral domain, we constructed a simple three-state model that described the localization of VSVG in its three definable compartments: TGN, the lateral plasma membrane, and transport carriers between the TGN and plasma membrane, the latter representing cytoplasmic volume that was not associated with the TGN or the lateral membrane (Fig. 1 D, open circles; the line is nonlinear because of its multicomponent nature). As illustrated in Fig. 2, two forward rate constants were used to fit the data (model 1): k_1, the rate of exit from the TGN, and k_2, the rate of exit from the transit compartment. k_1 and k_2 were determined by measuring the rate of exit from the TGN and arrival at the lateral domain, which was defined to include the cell margin and an intracellular volume ~1.5 μm from the cell margin. Thus, k_2 describes the duration of VSVG in the transit compartment; i.e., the time required to transfer from the TGN to the plasma membrane but not docking and fusion to the membrane. The kinetic analysis indicated that exit from the TGN was rate limiting (k_1 = 0.019 min^{-1}), with 1.9% of the VSVG-YFP exiting the TGN per minute, which is approximately equal to the first-order rate measured using a linear fit to the TGN exit curve. k_2 was ~10 times faster than TGN exit (Fig. 2; n = 12 cells), indicating that once in transit, VSVG was rapidly transferred to the lateral domain. The Golgi exit rate was comparable with that measured in nonpolarized COS cells by Hirschberg et al. (1998).

Previous studies have suggested that basolateral traffic is initially targeted to a site near the junctional complex and possibly even subjected to sorting from apical proteins upon delivery (Louvard, 1980; Grindstaff et al., 1998; Kreitzer et al., 2003). Therefore, we analyzed our dataset to determine whether there was evidence for a transient accumulation of VSVG-YFP at the junction-associated region or any other subdomain of the lateral membrane. We modified the kinetic model to include a new rate k_3 that would describe possible processes restricted to the junctional complex region (Fig. 2, model 2). Such events might include transport vesicle docking, vesicle fusion, sorting of apical versus basolateral proteins, or exit from the junction-associated

Model 1

TGN $\xrightarrow{k_1}$ **Intermediate Transit** $\xrightarrow{k_2}$ **Plasma Membrane**

	VSVG-YFP (n = 12)	GPI-GL-YFP (n = 9)
Exit rate from TGN; k_1 (min^{-1})[a]	0.019 ± 0.003	0.023 ± 0.004
Rate of delivery; k_2 (min^{-1})[a]	0.23 ± 0.06	0.07 ± 0.01

[a]Mean ± SEM.

Model 2

TGN $\xrightarrow{k_1}$ **Intermediate Transit** $\xrightarrow{k_2}$ **Junction-Associated Region** $\xrightarrow{k_3}$ **Plasma Membrane**

Model 3

TGN $\xrightarrow{k_1}$ **Intermediate Transit** $\xrightarrow{k_2}$ **Basolateral** $\xrightarrow{k_3}$ **Apical Membrane**

Figure 2. **The rate of exit from the TGN and delivery to the destined plasma membrane measured by live cell imaging.**

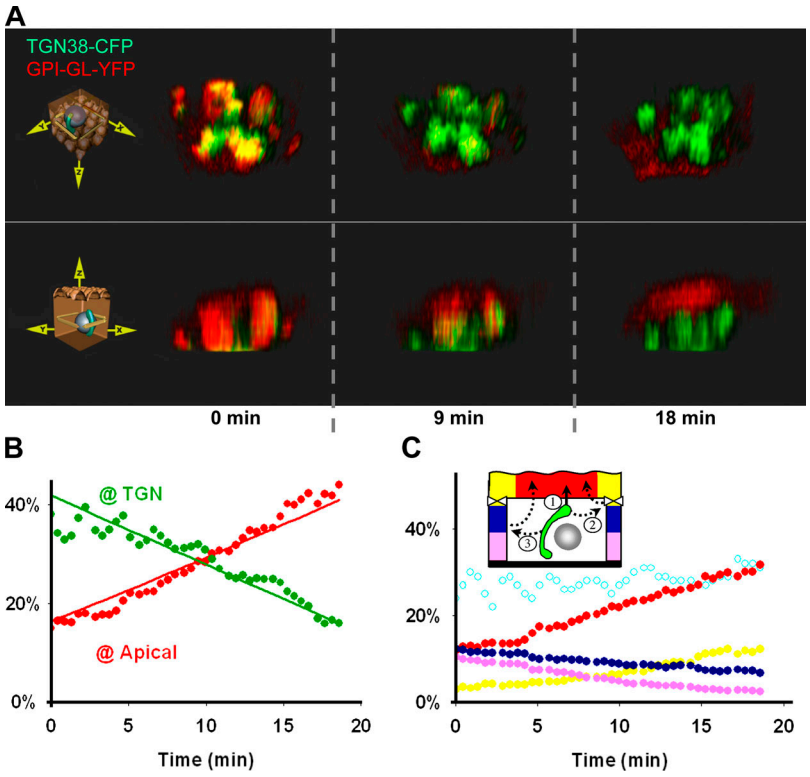

Figure 3. **3D transport of GPI-GL-YFP to the apical domain.** (A) 3D transport of newly synthesized GPI-GL-YFP (red) from the TGN (TGN38-CFP, green) to the apical membrane (including the underlying cytoplasmic volume within an ~2-μm distance from the cell margin) at various time points of chase at 31°C. Two different orientations of the same cell are illustrated (looking up from the basal side and from the lateral side). (B) Kinetics of GPI-GL-YFP transport from the TGN to the apical domain. The presence of GPI-GL-YFP in the TGN or in the entire apical domain was quantified at each time point from the 3D renderings. Global fit (solid lines) of the two-step pathway (Fig. 2, model 1) to the two curves yielded $k_1 = 0.02$ min^{-1}, $k_2 = 0.09$ min^{-1}, and $R^2 = 0.918$. (C) Spatial distribution of GPI-GL-YFP on the apical and lateral membranes. Appearance of GPI-GL-YFP in a central region of the apical membrane (red), defined as the region spanning half the distance from the cell axis to the cell margin (and the underlying volume, as described above), was compared with the appearance of fluorescence at the perimeter of the apical domain, which also contained one third of the lateral domain (yellow). Each data point corresponds to the percentage of GPI-GL-YFP that is distributed in the corresponding section of the diagram at each time point. The Xs demarcate the approximate location of the tight junction. Open cyan circles represent signal not accounted for at the apical or lateral domains or at the TGN. The dimensions of the cell image shown (x, y, and z) are ~11, 6, and 10 μm.

region (via diffusion or vesicular transport). At steady state, the amount of VSVG that accumulated in the junction-associated region would thus depend exclusively on k_2 and k_3. If this junctional region was the unique site to which post-TGN carriers were targeted, we might expect a transient accumulation of VSVG in that segment of the lateral domain.

To test this hypothesis, we measured the appearance of VSVG-YFP in three equal vertical, circumferential segments of the lateral membrane. The most apical section contained the junctional complex, as confirmed by staining with the tight junction marker ZO-1 (unpublished data). Contrary to expectations, however, VSVG-YFP did not appear preferentially in this upper segment. Fluorescence instead appeared in the bottom two lateral segments at equivalent rates (Fig. 1 D, red and blue dots). The same trend was observed for the apical-most segment (Fig. 1 D, yellow dots), although the amount of signal was reduced because this segment likely also contained a portion of the apical domain (above the junctional complex). Nevertheless, if all of the VSVG represented by the yellow dots (Fig. 1 D) reflected accumulation in the junction-associated region, the quantity was far less than predicted for preferential targeting (Fig. 1 D, dashed line). To fit the actual data to model 2 (Fig. 2), k_3 would need to be ≥ 1.6 min^{-1} (corresponding to $t_{1/2}$ of <26 s). k_3 is unlikely to be that fast because our previous study using glass-grown cells found that the docking of post-TGN VSVG-containing transport vesicles is considerably slower than 1.6 min^{-1} ($k = 1.1$ min^{-1}; $t_{1/2}$ of 39 s; Toomre et al., 2000). Thus, despite the possible restriction of vesicle-tethering complexes close to the junctional complex (Grindstaff et al., 1998), VSVG-YFP is delivered to a broad area of the lateral domain or, alternatively, the docking and fusion of vesicles at a restricted region is far faster than observed for other closely related events.

Next, we studied the intracellular transport of a newly synthesized apical membrane protein, GPI-GL-YFP, which is the same construct also used by Polishchuk et al. (2004). Newly synthesized GPI-GL-YFP was accumulated in the TGN by a 1-h temperature block at 20°C (Polishchuk et al., 2004), released at 31°C, and imaged at 1-min intervals in three dimensions (Videos 2 and 3, available at http://www.jcb.org/cgi/content/full/jcb.200512012/DC1). GPI-GL-YFP (Fig. 3 A, red) migrated out from the TGN region (Fig. 3 A, green) and appeared at the apical surface, which is defined as red pixels that were within ~2 μm of the apical cell margin (Fig. 3 A; 0, 9, and 18 min of chase; see Image and data processing). Transport was largely complete within 20 min. Importantly, no GPI-GL-YFP was observed visually at the lateral membrane at any time point. There was, however, an intermediate time when GPI-GL-YFP appeared as a region or compartment juxtaposed apically to the TGN (Videos 4 [~12 min] and 5). This region could correspond to a subdomain of the TGN or a subapical compartment containing presorted GPI-anchored molecules (Hannan et al., 1993). In any event, the video data strongly suggested a simple model in which GPI-GL-YFP migrates upward out of the TGN through an intermediate subapical domain and reaches the apical surface without ever appearing basolaterally.

We then quantified the kinetics of GPI-GL-YFP transport from the TGN to the apical regions. As shown in Fig. 3 B, the amount of GPI-GL-YFP in the TGN region decreased in accordance with the increase in the amount of GPI-GL-YFP at the apical membrane (green and red dots, respectively). The simplest three-state model (Fig. 2, model 1) accurately represented the

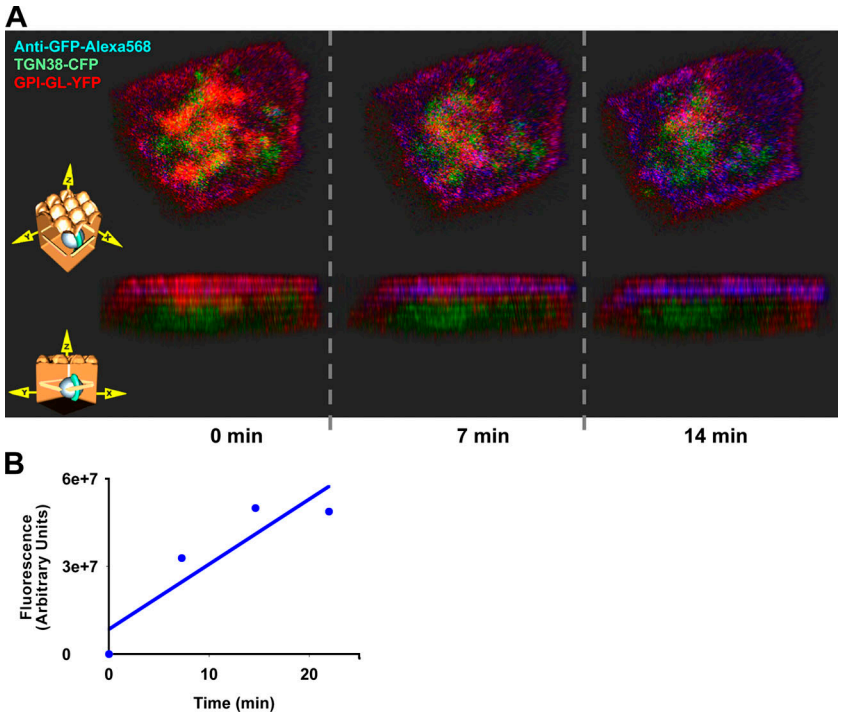

Figure 4. **Antibody-binding assay to detect the delivery of GPI-GL-YFP to the apical surface.** (A) The delivery of GPI-GL-YFP (red) from the TGN (TGN38-CFP, green) to the apical domain in a live fully polarized MDCK cell was imaged as in Fig. 3 except that a conjugated anti-GFP antibody (blue) was added to the apical medium. GPI-GL-YFP molecules appearing apically became accessible to the antibody, which concentrated at the apical surface. Two different orientations of the same cell are illustrated (looking down from the apical side and from the lateral side). The cell at 7 min was also digitally sectioned in Video 5 (available at http://www.jcb.org/cgi/content/full/jcb.200512012/DC1) to expose the distribution of GPI-GL-YFP in the TGN and subapical regions. (B) Kinetics of anti-GFP accumulation at the apical membrane. Data points were determined from the quantitation of 3D renderings (same cell as in A) at each time point. The solid line is not a curve fit but rather represents the kinetics of GPI-GL-YFP apically. This was plotted based on model 1 using the kinetic parameters in Fig. 2 except that the peak fluorescence (normalization factor) was fitted to the data. The dimensions of the cell image (x, y, and z) are ~10, 13, and 8 μm.

transport data (Fig. 3 B, solid green and red lines). Again, the rate-limiting step along the apical pathway was exit from the TGN. At 0.023 min^{-1} (2.3% GPI-GL-YFP transferred out of the TGN per minute), this rate was similar to that derived for the TGN exit of VSVG-YFP (Fig. 2; $n = 9$ cells).

To test quantitatively whether GPI-GL-YFP was delivered to the junctional region or the lateral domain before appearing apically (Fig. 3 C, inset; models 2 and 3), we determined the distribution of GPI-GL-YFP at each time point in the reconstructed 3D datasets. We first compared the appearance of GPI-GL-YFP in the apical membrane (choosing a segment ~2.5 μm from the cell lateral margin to avoid any contribution of the lateral domain; Fig. 3 C, inset; red) versus a perimeter segment including the edge of the apical membrane, the junctional region, and the apical-most segment of the lateral membrane (Fig. 3 C, inset; yellow). GPI-GL-YFP accumulated in both regions with similar kinetics (Fig. 3 C, red and yellow dots), but far more GPI-GL-YFP accumulated in the delimited apical region despite being a smaller volume. As with our analysis of VSVG-YFP transport, the only way model 2 could be consistent with the data is if the junctional residence of GPI-GL-YFP was so short as to be experimentally undetectable (k_3 of >4 min^{-1}). This is also unlikely because the newly delivered GPI proteins are immobile on the apical surface (Hannan et al., 1993) and should diffuse from a lateral insertion site slowly, enabling their detection. Thus, it seems unlikely that GPI-GL-YFP is inserted at the apical margin or the junction-associated region.

Although not visually obvious, a small fraction of GPI-GL-YFP was quantified as residing at the lower two segments of the lateral membrane at the start of the 31°C chase; this amount decreased with the time of chase (Fig. 3 C, blue and pink dots). However, this behavior was not consistent with a major indirect route to the apical membrane (Fig. 2 and Fig. 3 C, inset; model 3). Such a mechanism was calculated to require a flat or slightly increasing curve for the amount of lateral GPI-GL-YFP during the 20-min time course used here, which is inconsistent with the data. We suspect that the lateral GPI-GL-YFP reflected a partial missorting as expected (Keller et al., 2001; Paladino et al., 2004). Although it is possible that the lateral GPI-GL-YFP proceeded by transcytosis to the apical side, which is consistent with previous results (Polishchuk et al., 2004), the kinetic analysis is inconsistent with it being an obligatory intermediate on the apical pathway for the entire newly synthesized cohort.

At all times of chase, ~20% of GPI-GL-YFP fluorescence was localized neither to the TGN region nor to the apical (or lateral) membrane. Instead, it was distributed intracellularly underneath the apical membrane (Fig. 3 C, open circles). This signal may represent GPI-GL-YFP in equilibrium with endosomes in the apical cytoplasm. Therefore, it was important to determine whether the GPI-GL-YFP that appeared in the apical region had actually fused with the apical membrane. We repeated the experiment with fluorescent anti-GFP antibody in the medium (accessible to both apical and basolateral membranes). The insertion of GPI-GL-YFP will expose the extracellular YFP domain to the medium, enabling concentration of anti-GFP at the plasma membrane. Indeed, as GPI-GL-YFP was sorted away from TGN38-CFP and delivered toward the apical domain, it was accompanied by a steadily increasing amount of anti-GFP labeling on the apical membrane (Fig. 4 A). No significant anti-GFP labeling in the basolateral domain was detected, again indicating that little GPI-GL-YFP was inserted in the basolateral membrane. The total amount of antibody on the apical membrane increased with time, and the rate of insertion in the apical domain was in agreement with the kinetic data derived from quantifying GPI-GL-YFP fluorescence (Fig. 4 B).

In MDCK cells, the TGN may exhibit an overall expansion in surface area as a result of the 20°C block (Griffiths et al., 1985; Ladinsky et al., 2002). Because of this, upon shifting to 31°C, the TGN returns to its original size, perhaps slowing the initial rates of exit. Therefore, we measured the TGN exit rate of VSVG-YFP in the absence of a 20°C block. VSVG-YFP was accumulated in the ER at 40°C and was released by shifting directly to 31°C. The colocalization of VSVG-YFP with TGN38-CFP was used to estimate entry and exit from the TGN. Indeed, the rate of exit under these conditions ($0.008 \pm 0.002\ min^{-1}$; $n = 2$) was somewhat slower as compared with the exit rate after the 20°C block (Fig. 2). This suggests that after the 20°C block, VSVG exit from TGN may occur normally, with the faster rate perhaps reflecting the accumulation of VSVG in the TGN (Griffiths et al., 1985). To further characterize the effect of the 20°C block on VSVG-YFP exit from the TGN, rates were calculated from the first and last 10 min of our complete dataset ($n = 12$). On average, the rate calculated for the last 10 min was 17% slower, which is also inconsistent with the possibility that VSVG exit is slowed after 20°C block. When this analysis was performed for GPI-GL-YFP exit, we found that the initial rate was somewhat slower in three of nine cells (e.g., the initial lag in Fig. 3 B; green line), perhaps reflecting the time required for partitioning of GPI-anchored proteins into lipid microdomains before TGN exit (Paladino et al., 2004; Schuck and Simons, 2004).

To avoid the issue of temperature blocks entirely, we developed an assay to monitor transport kinetics at steady state and to assess independently the contribution of basolateral to apical transcytosis to GPI-GL-YFP targeting. For this purpose, we determined the binding and transport of anti-GFP antibody that was vectorially added to the basolateral or apical media of filter-grown cells. GPI-GL-YFP at both surfaces was first blocked with nonfluorescent anti-GFP IgG for 2 h. Cells were then incubated with anti–GFP-AlexaFluor647 in the basolateral medium for 30 min at 37°C (Fig. 5 A, diagram; blue antibody). Blue antibody detected by 3D imaging at the apical surface would, therefore, reflect GPI-GL-YFP transcytosis. At the end of the chase (at 0°C), anti–GFP-AlexaFluor594 (Fig. 5 A, diagram; red antibody) was added to the apical medium to detect GPI-GL-YFP molecules that had failed to bind the blue antibody (i.e., the population of GPI-GL-YFP that had not been exposed to the basolateral medium). As expected, the apical membrane was heavily labeled with AlexaFluor594 (red) antibody and was only slightly labeled with AlexaFluor647 (blue) antibody (Fig. 5 A). Thus, the majority of GPI-GL-YFP was apparently transferred directly from the TGN to the apical surface, as it did not bind anti-GFP in the basolateral medium. For reference, the TGN was indicated by TGN38-CFP (Fig. 5 A, green).

The digital reconstructions were used to quantify the relative contributions of direct versus transcytotic transport by determining the ratio of the two antibodies at the apical surface. To eliminate any bias caused by the differences in detection or binding of the two antibodies, we also collected datasets in which the antibodies were reversed. In either event, $<5\%$ of GPI-GL-YFP on the apical membrane came via the transcytotic pathway (i.e., had been tagged by the basolateral antibody; Fig. 5 C). The result was independent of the antibody concentration, indicating that anti-GFP saturated the membrane-bound GPI-GL-YFP. The same result was obtained if the cells were blocked for 1 h at 20°C, as in the imaging experiments (Fig. 3).

As a positive control to show that established transcytosis markers could be labeled on the basolateral surface while en route to their final destination (the apical surface), we tested cells expressing NgCAM-GFP (Anderson et al., 2005). Cells were incubated with anti–NgCAM-AlexaFluor647 (Fig. 5 B, blue antibody) in the basolateral medium for up to 90 min at 37°C (transcytosis of NgCAM takes ~90 min, which is slower than the apical appearance of GPI-GL-YFP; Anderson et al., 2005). The cells were cooled to 0°C, and anti–NgCAM-AlexaFluor594 (Fig. 5 B, red antibody) was then added to the apical medium to detect any NgCAM that had been directly inserted apically. The blue antibody labeled both the apical and lateral surfaces as well as a variety of intracellular endosomal compartments, which is consistent with transcytosis (Fig. 5 B). Only a small amount of red antibody bound to the apical surface. Quantitation of red versus blue revealed that $>95\%$ of the apical NgCAM-GFP had captured antibody in the basolateral medium (Fig. 5 C).

Discussion

3D imaging of living filter-grown MDCK cells has finally permitted a quantitative analysis of the rate and spatial restriction of domain-specific membrane protein transport in polarized epithelial cells. To image entire pathways, however, it was necessary to collect data over an ~30-min time course, requiring that frames be taken at relatively long (1 min) intervals to minimize photobleaching. Although interstack time intervals were too long to monitor individual transport vesicles, we did demonstrate unambiguously that at least two well-described apical and basolateral proteins were sorted intracellularly and inserted with a high degree of fidelity directly into their respective domains. Our visual and computed results confirm several early biochemical studies on traffic in polarized MDCK cells (Matlin and Simons, 1984; Griffiths et al., 1985; Pfeiffer et al., 1985; Lisanti et al., 1989; Casanova et al., 1991; Vieira et al., 2005), conclusions that were recently questioned based on immunofluorescence studies of vectorially fixed (and therefore highly perturbed) cells, using the same constructs as used here (Nelson and Rodriguez-Boulan, 2004; Polishchuk et al., 2004).

Some interesting differences were revealed between the apical and basolateral pathways. Although VSVG-YFP and GPI-GL-YFP had comparable exit rates from the TGN, the overall rate of exit from the transit compartment and apical delivery was demonstrably slower in the case of GPI-GL-YFP. One reason for this may be the appearance of a subapical intermediate compartment that accumulated GPI-GL-YFP at equilibrium. Similar compartments have been previously noted and termed apical endosomes or vacuolar-apical compartments, and they do appear to play a role in the endocytosis and recycling of apical components or as a biosynthetic transport intermediate (Vega-Salas et al., 1987; Casanova et al., 1999; Sheff et al., 1999; Brown et al., 2000). No such kinetic intermediate was observed on the basolateral pathway. Given the limited time resolution

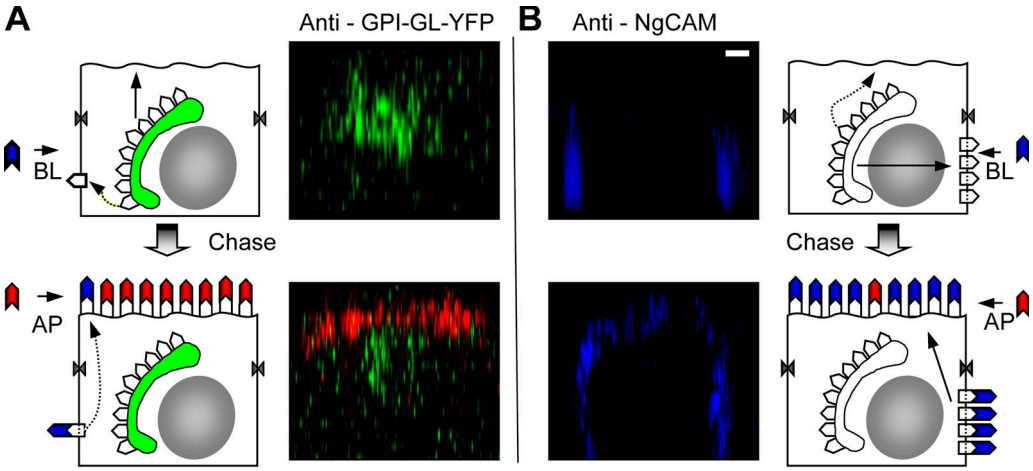

C

Fraction of new apical proteins that captured antibody at basolateral surface

	1x antibody	3x antibody
GPI-GL-YFP	4.8% ± 0.3%	3.5% ± 1.0%
NgCAM-GFP	95% ± 2%	n.d.

Figure 5. **Quantification of GPI-GL-YFP and NgCAM-GFP transyctosis.** (A) Cells were transfected with TGN38-CFP (green) and GPI-GL-YFP overnight and incubated with unconjugated anti-GFP antibody added to the apical (AP) and basal (BL) media for 2 h. The cells were then chased from 30 min with a blue antibody–conjugated anti-GFP added only to the basal medium. After washing, the cells were transferred to ice, and a red antibody–conjugated anti-GFP was added to the apical medium to detect free GPI-GL-YFP molecules. Complete 3D datasets were collected, and axial cross section images of representative cells are shown. Apical GPI-GL-YFP was poorly labeled by the blue antibody and heavily labeled by the red antibody, suggesting that few GPI-GL-YFP molecules ever gained access to the basal medium. Note that images acquired before and after chase represent different cells. Solid arrows illustrate the major route or transport, whereas dotted arrows illustrate the minor or insignificant routes. (B) Cells were transfected with NgCAM-GFP and were treated as in A except using an antibody to the NgCAM extracellular domain and that chase times were for 90 min. In this case, apical NgCAM was significantly labeled by the blue antibody, which was encountered in the basal medium. The absence of red antibody binding indicated that few free NgCAM molecules were accessible, suggesting that most of the NgCAM reached the apical surface after first appearing at the basolateral surface. Note that images acquired before and after chase represent different cells. Bar, 2 μm. (C) Based on quantification of the amount of antibody labeling on the apical domain, the percentage of GPI-GL-YFP and NgCAM-GFP that had been exposed to the basolateral domain was measured. For GPI-GL-YFP, two different antibody-labeling concentrations were used to ensure saturation.

used in this study, we would not have expected to detect the transit of VSVG or GPI-GL-YFP through recycling endosomes (Ang et al., 2004) unless this step was similarly rate limiting (i.e., $<0.23\ min^{-1}$). It apparently was not. The apical endosomal compartment may accumulate GPI-GL-YFP because of its ability to partition into relatively immobile lipid microdomains that may be abundant in these compartments (Gagescu et al., 2000; Paladino et al., 2004; Schuck and Simons, 2004).

The processes of vesicle docking and fusion were not studied in detail. For VSVG, we could not distinguish whether VSVG transporters were docked versus fused with the lateral membrane. Increased time resolution alone would certainly permit the tracking of individual vesicles, as accomplished by Kreitzer et al. (2003). However, from the point of view of establishing kinetics, such an analysis would not help. At present, there is no way to judge definitively that fusion of a single vesicle has occurred at the lateral surface, which cannot yet be studied by total internal reflectance microscopy. In our dataset, appearance at the lateral membrane represents the aggregate rate of docking and fusion followed by rapid diffusion of VSVG in the lipid bilayer.

As a result, we cannot definitively rule out the possibility that laterally targeted vesicles dock and fuse at a site close to the junctional complex. Because of the high mobility of VSVG on the lateral membrane, even if insertion is strictly limited to the junctional region, VSVG-GFP would appear evenly distributed on the lateral membrane in our experiments. However, the data do predict that if insertion at the junctional region is obligatory, the mean residence time at the junction (including docking, fusion, and diffusional exit) must be 26 s or less. Longer residence times, such as those measured for post-TGN VSVG-containing vesicles docking at the plasma membrane of glass-grown cells ($t_{1/2}$ of 39 s; Toomre et al., 2000), would have been detected.

Although our approach is certainly just a methodological beginning to the problem of elucidating the kinetic and spatial control of membrane traffic in complex cells, it has permitted a definitive resolution of the vectorial nature of biosynthetic protein transport in MDCK cells, which is one of the oldest and most fundamental problems in the field. Clearly, the approach will lend itself to other cargos and cell types, especially cells that have been manipulated to exhibit the reduced expression of candidate genes involved in polarity or transport.

Materials and methods

Microscopy

A confocal laser scanning inverted microscope (LSM-510; Carl Zeiss MicroImaging, Inc.) with a temperature-controlled stage set at 31°C was used for image acquisition. To minimize refractive index mismatch, we used

a 40× NA 1.2 water immersion lens (Carl Zeiss MicroImaging, Inc.) with temperature and coverslip thickness correction. To achieve quantitative 3D live cell imaging of the entire sorting pathway that takes ~30 min, with minimum photobleaching of the fluorescence, the excitation laser power was adjusted to instrument minimum (0.1%), and the maximum laser scanning speed was used. It took 2–30 s (typically 15 s) to complete 6–10 z stacks of a single cell at ~1 μm per image, depending on the number of fluorescent channels to scan (typically four), the size of the scanning areas (typically 50–100 μm), and the number of scanning repeats (typically two). Pinhole size was increased up to 4 Airy units to increase light collection without significant background noise from stray light. Image resolution is independent of pinhole size under these conditions. Total photobleaching of our CFP and YFP probes (see next section) under these conditions was ≤40% (see Fig. S1). The detectors (photomultiplier tubes) were adjusted to maximally amplify but not saturate the signal. The collected digital signals were proportional to the photon input (LSM-510; Carl Zeiss MicroImaging, Inc.), which was, to the first order, proportional to the amount of fluorescent proteins being illuminated in a given area. To compensate for the slow z drift during the course of recording, the Zeiss software package was used to automatically correct the focus every 3 min according to the z position of the filter on which the MDCK cells were grown.

Tissue cell culture, protein expression, and antibodies

Standard MDCK II cells or MDCK II that stably expressed human transferrin receptor (Sheff et al., 1999) were cultured under standard procedures (Hunziker et al., 1991); i.e., incubated at 5% CO_2 in DME with 10% FCS and 1× glutamine. TGN38-CFP, VSVG-SP-YFP (abbreviated here as VSVG-YFP), GPI-GL-YFP, NgCAM-GFP constructs, and anti-NgCAM antibody were described previously (Toomre et al., 2000; Keller et al., 2001; Ang et al., 2003; Anderson et al., 2005). Anti-GFP antibody labeled with AlexaFluor594 and 647 was obtained from Invitrogen. Anti-NgCAM was labeled with AlexaFluor568 and 647 with the Zenon Antibody Labeling Kit (Invitrogen). For microscopy experiments, MDCK cells were seeded at 2×10^6 cells/well on polycarbonate transwell filters (clear type; Corning) in six-well plates. 56 h later, cells were transfected with 2–3 μg DNA per well using LipofectAMINE 2000 (Invitrogen) according to the manufacturer's instructions and incubated at 40°C (except for transcytosis assays, which were performed at 37°C). The 40°C overnight incubation blocked the temperature-sensitive (ts045) VSVG-YFP in the ER but not GPI-GL-YFP or NgCAM-GFP. Imaging was performed ~16 h after transfection.

Time-series microscope experiment

MEM medium without phenol red (Invitrogen) was supplemented with 10 mM Hepes and used for all microscope experiments (MEM-H). A 35-mm petri dish (Matek) containing a coverslip bottom was precleaned with ethanol. A piece of filter was cut off (together with a patch of cells grown on top) and placed on the coverslip with cells facing down the coverslip. A custom-made three prop weight was put on top of the filter–cell complex for sample stabilization while enabling free medium exchange for the cells through the space between the cells and the coverslip (Fig. 1 A). Cells were viable for >12 h. All of the cells recorded (total number indicated in Fig. 2) showed behavior and kinetics similar to those shown in Figs. 1 and 3. For all assays (except the transcytosis assay), the incubation medium was MEM-H. When needed, the medium was supplemented with 33 ug/ml transferrin-AlexaFluor568 and 250 μg/ml dextran-AlexaFluor647 or 3 μg/ml anti-GFP antibodies. Transferrin and dextran were used to label the recycling endosomes and lysosomes, respectively, and VSVG transport rates in MDCK cells expressing human transferrin receptors was indistinguishable to normal MDCK cells. Cells were incubated at 40°C with MEM-H for 1 h and blocked at 20°C for 1 h to accumulate cargo (VSVG-YFP and GPI-GL-YFP) in the TGN. GPI-GL-YFP that was already on the apical surface was removed by 0.8 ug/ml phosphatidylinositol-specific PLC (Sigma-Aldrich) treatment for 30 min at 20°C in PBS supplemented with 100 μg/ml Ca^{2+} and Mg^2. The time from the placement of the cells in 31°C medium to the start of the image acquisition was recorded (t_0) and was typically between 3–20 min. Live cell microscope experiments (except for the transcytosis assay) were performed at 31°C with 20 μg/ml cycloheximide to inhibit new protein synthesis (Ang et al., 2003).

Transcytosis assay

Cells were incubated with 50 μg/ml of unlabeled antibody in both the apical and basolateral medium for 2 h at 37°C, washed, and chased with 10 μg/ml AlexaFluor594 (or AlexaFluor568)-labeled antibody in basolateral medium. The chase time was 30 min for the GPI-GL-YFP experiment and 90 min for the NgCAM-GFP experiment to account for the slow transcytosis of NgCAM (Anderson et al., 2005). Cells were washed, and a 10× dilution of the Zenon Kit (Invitrogen) blocker reagent was added to the apical medium and incubated for 10 min. Cells were washed, and 10 μg/ml AlexaFluor647-labeled antibody was added to the apical medium and incubated for 5 min. Cells were then incubated in antibody-free medium for 10 min at 0°C, and the filter–cell complex was cut off and imaged at <20°C without fixation. The duration of the microscope experiment was <10 min, and the pattern of the antibody labeling was unchanged during the time. Similar results were obtained with 4% PFA-fixed cells except that the cells slightly deformed in the axial direction as a result of fixation, and the autofluorescent background was higher. For the GPI-GL-YFP transcytosis assay, the antibody concentration described was referred to as 3× in the text. The experiment with the AlexaFluor647 antibody used in the basolateral medium and AlexaFluor594 (or AlexaFluor568) in the apical medium were performed simultaneously under otherwise identical conditions.

Image and data processing

Images were processed and quantified with LSM-510 software (Carl Zeiss MicroImaging, Inc.), and Volocity with the visualization and classification modules (Improvision). Slight submicrometer spatial spectral shifts were sometimes observed and corrected using the software shift function. Background noise (e.g., the fluorescent signal in neighboring cells not expressing GFP or its color variant) was minimal when optimal gain/offset settings for the detectors were used. No nonlinear algorithms were used to alter the quantification of the fluorescent signals, so the final signals were proportional to the amount of fluorescent proteins. In some cases, the reflection of the laser from the filter creates wide-spectrum noise at the z sections close to the filter, and the affected sections were removed from further processing. The definition of cellular structures are as follows: the TGN region was defined by the 3D TGN38-CFP image through the classification process in Volocity. Specifically, an intensity threshold was first applied to eliminate background fluorescence followed by a medium spatial filter to smooth the image. Background signal was further rejected using particle size threshold to exclude particles that were <0.06 μm^3. The resulting fluorescent volume was used to represent the TGN structure; its fluctuation was <20% over 20 min. The boundary of the cell of interest (that expresses both CFP and YFP) was determined by the increased background fluorescence level in the target cell. The apical domain was defined as the top 25% of the cell image minus the TGN region if there was any overlap. The lateral domain was defined as the volume from the cell's lateral edge to approximately two thirds of the distance from the cell's center vertical axis minus the TGN and apical regions. For kinetic measurements, at every time point, the total fluorescent signal of the transport cargo proteins (GPI-GL-YFP and VSVG-YFP) in the defined structures (such as the TGN) was quantified, and the final signal was calculated by the fluorescent signal in that structure divided by total fluorescent signal in the whole cell. In the transcytosis assay, we measured total fluorescence on the apical domain because of antibody added to the apical (F_a) or basolateral medium (F_b) and calculated the ratio $k' = F_b/F_a$. Two sets of the experiments—one with the AlexaFluor647 antibody in the basolateral medium and AlexaFluor594 (or AlexaFluor568) in the apical medium and the other with the antibody color swapped—were performed side by side. The geometric mean of the k′ measured from the two sets of experiments was calculated (k). The fraction of new apical proteins that captured antibody at the basolateral surface was expressed by $k/(1 + k)$.

Kinetic measurements

The protein transport steps that we observed fit well with a simple two-step process (Fig. 2, model 1) in which the intermediate transit of proteins was detected as significant intracellular fluorescence outside of the TGN. Protein quantity in the TGN under the experimental condition $P_{TGN} = P_0 \times [1 - k_1 \times (t + t_0)]$, where P_0 is the initial protein quantity and t_0 is the duration between the start of the 31°C chase and the start of the recording, was described in Time-series microscope experiment. Protein quantity at the destination plasma membrane is $P_{PM} = P_0 \times [k_1 \times (t + t_0) - k_1/k_2 \times [1 - e^{-k_2 (t + t_0')}]]$ and in the intermediate transit is $P_{INT} = P_0 \times k_1/k_2 \times (1 - e^{-k_2 (t + t_0')}) + D$, where D is the fixed amount of intracellular labeling as a result of various background noise. Thus, the total fluorescence is $P_T = P_{TGN} + P_{PM} + P_{INT}$. P_{TGN}/P_T and P_{PM}/P_T were globally fitted to the experimental curves such as those in Figs. 1 C and 3 B (SigmaPlot software; Systat). D/P_T from all experiments was ≤35% (typically ~15%). In models 2 and 3, three steps with rates k_1, k_2, and k_3 are used. The last two states were first combined, and such a two-step process was fitted to the data to obtain k_1 and k_2 as described above. For model 2, $P_{JUN} = k_2/(k_3 - k_2) \times [P_{INT} - P_0 \times k_1/k_3 \times [1 - e^{-k_3 (t + t_0')}]]$ and $P_{PM} = P_0 \times k_1 \times (t + t_0) - P_{INT} - P_{JUN}$. $P_{blue + purple} = P_{PM} \times (1 - g)$ and $P_{yellow} = P_{JUN} + P_{PM} \times g$, where g is the proportion of the lateral membrane included in the yellow section (Figs. 1 D and 3 C), were fitted to the fluorescence in the blue + purple lateral

area and the yellow area, respectively. For model 3, $P_{BL} = k_2/(k_3 - k_2) \times [P_{INT} - P_0 \times k_1/k_3 \times [1 - e^{-k_3 (t + t_0)}]]$ and $P_{AP} = P_0 \times k_1 \times (t + t_0) - P_{INT} - P_{BL}$. In fitting the data to model 1, the degree of freedom-adjusted R^2 was 0.97 ± 0.03 for all of the nonlinear regression fits to the VSVG-YFP data and 0.92 ± 0.05 for all GPI-GL-YFP data. R^2 from fitting data to model 1 (two-step model) was statistically indistinguishable from the R^2 for fitting to models 2 and 3 (three-step models), suggesting that the simplest two-step model can explain the data as well as the three-step model; thus, introducing another parameter, k_3, can be unnecessary.

Online supplemental material

Fig. S1 shows the quantitation of total fluorescence signal (Fig. 1, dataset) used to correct for loss as a result of photobleaching. Video 1 is an animated 3D video of Fig. 1. Videos 2–4 are animated 3D videos of Fig. 3. Video 5 shows an illustration of the post-TGN subapical accumulation of GPI-GL-GFP. Online supplemental material is available at http://www.jcb.org/cgi/content/full/jcb.200512012/DC1.

We thank Graham Warren for invaluable suggestions on the experiment and manuscript; Eric Anderson, Sandra Mayday, and Agnes Ang for constructs, antibodies, and excellent discussions; Cécile Chalouni for expert advice with microscopy; Adam Hartley for superb graphic support; and Janet Lee, Melisa Carrasco, and Henry Tan for invaluable technical assistance.

This work is supported by the Jane Coffin Child's Fund to W. Hua and National Institutes of Health grants to I. Mellman (RO1-GM29765 and PO1-CA46128). I. Mellman is an Affiliate Member of the Ludwig Institute for Cancer Research.

Submitted: 2 December 2005
Accepted: 24 February 2006

References

Anderson, E., S. Maday, J. Sfakianos, M. Hull, B. Winckler, D. Sheff, H. Folsch, and I. Mellman. 2005. Transcytosis of NgCAM in epithelial cells reflects differential signal recognition on the endocytic and secretory pathways. *J. Cell Biol.* 170:595–605.

Ang, A.L., H. Folsch, U.M. Koivisto, M. Pypaert, and I. Mellman. 2003. The Rab8 GTPase selectively regulates AP-1B-dependent basolateral transport in polarized Madin-Darby canine kidney cells. *J. Cell Biol.* 163:339–350.

Ang, A.L., T. Taguchi, S. Francis, H. Folsch, L.J. Murrells, M. Pypaert, G. Warren, and I. Mellman. 2004. Recycling endosomes can serve as intermediates during transport from the Golgi to the plasma membrane of MDCK cells. *J. Cell Biol.* 167:531–543.

Bartles, J.R., H.M. Feracci, B. Stieger, and A.L. Hubbard. 1987. Biogenesis of the rat hepatocyte plasma membrane in vivo: comparison of the pathways taken by apical and basolateral proteins using subcellular fractionation. *J. Cell Biol.* 105:1241–1251.

Brown, P.S., E. Wang, B. Aroeti, S.J. Chapin, K.E. Mostov, and K.W. Dunn. 2000. Definition of distinct compartments in polarized Madin-Darby canine kidney (MDCK) cells for membrane-volume sorting, polarized sorting and apical recycling. *Traffic*. 1:124–140.

Casanova, J.E., Y. Mishumi, Y. Ikehara, A.L. Hubbard, and K.E. Mostov. 1991. Direct apical sorting of rat liver dipeptidylpeptidase IV expressed in Madin-Darby canine kidney cells. *J. Biol. Chem.* 266:24428–24432.

Casanova, J.E., X. Wang, R. Kumar, S.G. Bhartur, J. Navarre, J.E. Woodrum, Y. Altschuler, G.S. Ray, and J.R. Goldenring. 1999. Association of Rab25 and Rab11a with the apical recycling system of polarized Madin-Darby canine kidney cells. *Mol. Biol. Cell*. 10:47–61.

Folsch, H. 2005. The building blocks for basolateral vesicles in polarized epithelial cells. *Trends Cell Biol.* 15:222–228.

Folsch, H., H. Ohno, J.S. Bonifacino, and I. Mellman. 1999. A novel clathrin adaptor complex mediates basolateral targeting in polarized epithelial cells. *Cell*. 99:189–198.

Folsch, H., M. Pypaert, S. Maday, L. Pelletier, and I. Mellman. 2003. The AP-1A and AP-1B clathrin adaptor complexes define biochemically and functionally distinct membrane domains. *J. Cell Biol.* 163:351–362.

Gagescu, R., N. Demaurex, R.G. Parton, W. Hunziker, L.A. Huber, and J. Gruenberg. 2000. The recycling endosome of Madin-Darby canine kidney cells is a mildly acidic compartment rich in raft components. *Mol. Biol. Cell*. 11:2775–2791.

Gan, Y., T.E. McGraw, and E. Rodriguez-Boulan. 2002. The epithelial-specific adaptor AP1B mediates post-endocytic recycling to the basolateral membrane. *Nat. Cell Biol.* 4:605–609.

Griffiths, G., S. Pfeiffer, K. Simons, and K. Matlin. 1985. Exit of newly synthesized membrane proteins from the trans cisterna of the Golgi complex to the plasma membrane. *J. Cell Biol.* 101:949–964.

Grindstaff, K.K., C. Yeaman, N. Anandasabapathy, S.C. Hsu, E. Rodriguez-Boulan, R.H. Scheller, and W.J. Nelson. 1998. Sec6/8 complex is recruited to cell-cell contacts and specifies transport vesicle delivery to the basal-lateral membrane in epithelial cells. *Cell*. 93:731–740.

Hannan, L.A., M.P. Lisanti, E. Rodriguez-Boulan, and M. Edidin. 1993. Correctly sorted molecules of a GPI-anchored protein are clustered and immobile when they arrive at the apical surface of MDCK cells. *J. Cell Biol.* 120:353–358.

Hirschberg, K., C.M. Miller, J. Ellenberg, J.F. Presley, E.D. Siggia, R.D. Phair, and J. Lippincott-Schwartz. 1998. Kinetic analysis of secretory protein traffic and characterization of Golgi to plasma membrane transport intermediates in living cells. *J. Cell Biol*. 143:1485–1503.

Hunziker, W., C. Harter, K. Matter, and I. Mellman. 1991. Basolateral sorting in MDCK cells requires a distinct cytoplasmic domain determinant. *Cell*. 66:907–920.

Keller, P., D. Toomre, E. Diaz, J. White, and K. Simons. 2001. Multicolour imaging of post-Golgi sorting and trafficking in live cells. *Nat. Cell Biol.* 3:140–149.

Kreitzer, G., J. Schmoranzer, S.H. Low, X. Li, Y. Gan, T. Weimbs, S.M. Simon, and E. Rodriguez-Boulan. 2003. Three-dimensional analysis of post-Golgi carrier exocytosis in epithelial cells. *Nat. Cell Biol.* 5:126–136.

Ladinsky, M.S., C.C. Wu, S. McIntosh, J.R. McIntosh, and K.E. Howell. 2002. Structure of the Golgi and distribution of reporter molecules at 20 degrees C reveals the complexity of the exit compartments. *Mol. Biol. Cell*. 13:2810–2825.

Lipardi, C., L. Nitsch, and C. Zurzolo. 2000. Detergent-insoluble GPI-anchored proteins are apically sorted in fischer rat thyroid cells, but interference with cholesterol or sphingolipids differentially affects detergent insolubility and apical sorting. *Mol. Biol. Cell*. 11:531–542.

Lisanti, M.P., I.W. Caras, M.A. Davitz, and E. Rodriguez-Boulan. 1989. A glycophospholipid membrane anchor acts as an apical targeting signal in polarized epithelial cells. *J. Cell Biol.* 109:2145–2156.

Lisanti, M.P., I.W. Caras, T. Gilbert, D. Hanzel, and E. Rodriguez-Boulan. 1990. Vectorial apical delivery and slow endocytosis of a glycolipid-anchored fusion protein in transfected MDCK cells. *Proc. Natl. Acad. Sci. USA*. 87:7419–7423.

Louvard, D. 1980. Apical membrane aminopeptidase appears at site of cell-cell contact in cultured kidney epithelial cells. *Proc. Natl. Acad. Sci. USA*. 77:4132–4136.

Matlin, K.S., and K. Simons. 1984. Sorting of an apical plasma membrane glycoprotein occurs before it reaches the cell surface in cultured epithelial cells. *J. Cell Biol.* 99:2131–2139.

Matter, K., and I. Mellman. 1994. Mechanisms of cell polarity: sorting and transport in epithelial cells. *Curr. Opin. Cell Biol.* 6:545–554.

Matter, K., M. Brauchbar, K. Bucher, and H.P. Hauri. 1990. Sorting of endogenous plasma membrane proteins occurs from two sites in cultured human intestinal epithelial cells (Caco-2). *Cell*. 60:429–437.

Mostov, K., T. Su, and M. ter Beest. 2003. Polarized epithelial membrane traffic: conservation and plasticity. *Nat. Cell Biol.* 5:287–293.

Nelson, W.J., and E. Rodriguez-Boulan. 2004. Unravelling protein sorting. *Nat. Cell Biol.* 6:282–284.

Paladino, S., D. Sarnataro, R. Pillich, S. Tivodar, L. Nitsch, and C. Zurzolo. 2004. Protein oligomerization modulates raft partitioning and apical sorting of GPI-anchored proteins. *J. Cell Biol.* 167:699–709.

Pfeiffer, S., S.D. Fuller, and K. Simons. 1985. Intracellular sorting and basolateral appearance of the G protein of vesicular stomatitis virus in Madin-Darby canine kidney cells. *J. Cell Biol.* 101:470–476.

Polishchuk, R., A. Di Pentima, and J. Lippincott-Schwartz. 2004. Delivery of raft-associated, GPI-anchored proteins to the apical surface of polarized MDCK cells by a transcytotic pathway. *Nat. Cell Biol.* 6:297–307.

Rodriguez-Boulan, E., G. Kreitzer, and A. Musch. 2005. Organization of vesicular trafficking in epithelia. *Nat. Rev. Mol. Cell Biol.* 6:233–247.

Schuck, S., and K. Simons. 2004. Polarized sorting in epithelial cells: raft clustering and the biogenesis of the apical membrane. *J. Cell Sci.* 117:5955–5964.

Sheff, D.R., E.A. Daro, M. Hull, and I. Mellman. 1999. The receptor recycling pathway contains two distinct populations of early endosomes with different sorting functions. *J. Cell Biol.* 145:123–139.

Sheff, D.R., R. Kroschewski, and I. Mellman. 2002. Actin dependence of polarized receptor recycling in Madin-Darby canine kidney cell endosomes. *Mol. Biol. Cell*. 13:262–275.

Simmen, T., S. Honing, A. Icking, R. Tikkanen, and W. Hunziker. 2002. AP-4 binds basolateral signals and participates in basolateral sorting in epithelial MDCK cells. *Nat. Cell Biol.* 4:154–159.

Toomre, D., J.A. Steyer, P. Keller, W. Almers, and K. Simons. 2000. Fusion of constitutive membrane traffic with the cell surface observed by evanescent wave microscopy. *J. Cell Biol.* 149:33–40.

Vega-Salas, D.E., P.J. Salas, D. Gundersen, and E. Rodriguez-Boulan. 1987. Formation of the apical pole of epithelial (Madin-Darby canine kidney) cells: polarity of an apical protein is independent of tight junctions while segregation of a basolateral marker requires cell-cell interactions. *J. Cell Biol.* 104:905–916.

Vieira, O.V., P. Verkade, A. Manninen, and K. Simons. 2005. FAPP2 is involved in the transport of apical cargo in polarized MDCK cells. *J. Cell Biol.* 170:521–526.